Journal of Geodesy manuscript No.
(will be inserted by the editor)

Least-squares cross wavelet analysis and its applications in geophysical time series

Ebrahim Ghaderpour[1] · **E. Sinem Ince**[2] · **Spiros D. Pagiatakis**[3]

Abstract The least-squares wavelet analysis, an alternative to the classical wavelet analysis, was introduced in order to analyze unequally spaced and non-stationary time series exhibiting components with variable amplitude and frequency over time. There are a few methods such as cross wavelet transform and wavelet coherence that can analyze two time series together. However, these methods cannot generally be used to analyze unequally spaced and non-stationary time series with associated covariance matrices that may have trends and/or datum shifts. A new method of analyzing two time series together, namely, the least-squares cross wavelet analysis, is developed and applied to study the disturbances in the gravitational gradients observed by GOCE satellite that arise from plasma flow in the ionosphere represented by Poynting electromagnetic energy flux. The proposed method also shows its outstanding performance on the Westford-Wettzell very long baseline interferometry baseline length and temperature series.

[1] Ebrahim Ghaderpour*
E-mail: ebig2@yorku.ca

[2] E. Sinem Ince
E-mail: seince@yorku.ca

[3] Spiros D. Pagiatakis
E-mail: spiros@yorku.ca

[1,2,3] Department of Earth and Space Science and Engineering, Lassonde School of Engineering, York University, Toronto, ON, Canada M3J1P3.

[1] *Department of Mathematics and Statistics, University of Calgary, Calgary, AB, Canada T2N1N4*
E-mail: ebrahim.ghaderpour@ucalgary.ca

[2] *Helmholtz Centre Potsdam GFZ German Research Centre for Geosciences Telegrafenberg, D-14473, Potsdam, Germany*
E-mail: elmas.sinem.ince@gfz-potsdam.de

Keywords Coherency · Cross-spectrogram · GOCE · Gravity field · Least-squares wavelet analysis · Time series · Unequally spaced series · Unequally weighted series · VLBI

1 Introduction

In many areas such as astronomy, geodesy, geophysics, meteorology and glaciology, researchers usually deal with non-stationary time series that are unequally spaced and unequally weighted exhibiting data gaps, trends and/or datum shifts (Wells et al. 1985; Brown and Hwang 2012). It is not unusual to see that researchers attempt to modify or edit the time series under consideration to satisfy the well-established standard methods, such as Fourier transform and continuous wavelet transform (Mallat 1999) by using, for instance, interpolation to fill in the data gaps in the series. However, such modifications may cause significant biases in the spectral peaks especially when the time series is non-stationary (Kay and Marple 1981).

Foster (1996) proposed a novel approach for analyzing astronomical time series that are unequally spaced. His method, namely, the weighted wavelet Z-transform (WWZ), is defined in terms of the estimated signal to noise ratio using the least-squares method. Thereafter, several other effective methods of analyzing non-stationary and unequally spaced time series have been proposed (Mathias et al. 2004; Amato et al. 2006).

The least-squares wavelet analysis (LSWA) is a new method of analyzing non-stationary time series that may be equally or unequally spaced (Ghaderpour and Pagiatakis 2017). The LSWA is based on the well-known least-squares spectral analysis (LSSA) introduced by Vanicek (1969) but expanded to the time-frequency domain. As such, the LSWA has all the desired properties of the LSSA and can be applied to any unequally spaced and non-stationary time series without any editing. More importantly, the LSWA computes a normalized least-squares wavelet spectrogram (LSWS), that is, the values of spectral peaks in the spectrogram are between zero and one. The LSWA calculates the spectrogram of a time series by fitting sinusoidal base functions to segments of the time series, and so it decomposes the time series into the time-frequency domain. The LSWA and WWZ are both excellent methods in determining the periodicities of constituents in a time series because they are least-squares based. The LSWA is defined in terms of the ratio of the estimated signal to the sum of the estimated signal and noise which allows one to search for hidden signals in a time series.

In many applications, researchers want to investigate the correlation or coherency between two time series, so that they can search for common constituents at different time segments. There are several methods proposed for analyzing two time series together such as the least-squares self-coherency analysis (Abd El-Gelil et al. 2008; Abd El-Gelil and Pagiatakis 2009) and the cross wavelet transform (Torrence and Compo 1998; Grinsted et al. 2004). The least-squares self-coherency analysis is based on the LSSA and is not suitable for analyzing time series that have variability of amplitude and frequency over time. On the other hand, the cross wavelet transform (XWT) is based on the continuous wavelet transform that is not defined for unequally spaced and unequally weighted time series.

In this contribution, we first revisit the LSWA to introduce the least-squares cross wavelet analysis (LSCWA). Then we derive the stochastic surfaces (confidence level surfaces) for the least-squares cross wavelet spectrogram (LSCWS) that show which peaks are statistically significant at a certain confidence level. We also discuss a special case of the LSCWA, called the least-squares cross spectral analysis (LSCSA), along with its least-squares cross spectrum (LSCS) and study the phase differences in the LSCWS and LSCS. We summarize the properties of these methods in Table 1.

We show the performance of our proposed method on two synthetic time series. The method is also applied to Gravity field and steady-state Ocean Circulation Explorer (GOCE) electrostatic gradiometer measurement disturbances to determine their coherence with the Poynting energy flux along two successive ascending satellite tracks during a magnetic storm (Ince and Pagiatakis 2016) to show its superior performance on the time series of different sampling rates. In another application, the coherency between the Very Long Baseline Interferometry (VLBI) baseline length series from Westford to Wettzell with the temperature series (recorded since 1984) is investigated to show the effect of the temperature variation on the baseline length.

2 Least-squares wavelet analysis revisited

In this section, the LSWA is briefly revisited and will be used in the cross analysis of two time series (for more details see Ghaderpour and Pagiatakis 2017). Suppose that $\mathbf{f} = \big[f(t_j)\big]$, $1 \le j \le n$, is a discrete time series of n data points; here the t_j's are not necessarily equally spaced. Let $\mathbf{\Omega} = \{\omega_k;\ k = 1, \ldots, \kappa\}$ be a set of spectral frequencies of interest. For each j, $1 \le j \le n$, and each k, $1 \le k \le \kappa$, define the segment of the time series corresponding to pair (t_j, ω_k) as

$$\mathbf{y} = \Big[f\big(t_{i+j-\frac{1}{2}(L(\omega_k)+1)}\big)\Big], \tag{1}$$

where $L(\omega_k)$ is a particular number depending on ω_k that we define later. Note that for each j and each k, i runs from 1 to $L(\omega_k)$ (except for the marginal segments), so segment $\mathbf{y}$ is a column vector of dimension $L(\omega_k)$. Now we use the sinusoidal base functions to define the following design matrix for pair (t_j, ω_k)

$$\mathbf{\Phi} = \Big[\cos\big(2\pi\omega_k t_{i+j-\frac{1}{2}(L(\omega_k)+1)}\big), \sin\big(2\pi\omega_k t_{i+j-\frac{1}{2}(L(\omega_k)+1)}\big)\Big]. \tag{2}$$

One may also use other base functions or wavelets to define the design matrix; however, we use the sinusoidal base functions to study the periodicity of the phenomena directly. In order to resolve the frequency ω_k for short duration signatures in the time series, we may define $L(\omega_k)$ as

$$L(\omega_k) := \begin{cases} \Big\lfloor \dfrac{L_1 M}{\omega_k} \Big\rfloor + L_0 & \text{if } \Big\lfloor \dfrac{L_1 M}{\omega_k} \Big\rfloor + L_0 \text{ is odd,} \\[2ex] \Big\lfloor \dfrac{L_1 M}{\omega_k} \Big\rfloor + L_0 + 1 & \text{otherwise,} \end{cases} \tag{3}$$

where symbol $\lfloor * \rfloor$ is the largest integer no greater than $*$, L_0 is a fixed number of data points, L_1 is a selected number of cycles of the sinusoidal base functions, M is a selected number of data points per unit time, and ω_k is the number of cycles per unit time ($\omega_k \in \mathbf{\Omega}$). For instance, for an equally spaced time series recorded in milliseconds, if frequency is in Hertz, then $M = 1000$ (data points per second), and if $L_1 = 2$, then two cycles of sinusoidal base functions of frequency ω_k will be fitted to a segment of the time series with $L(\omega_k)$ data points (see below). Also, L_0 is the selected number of

Table 1 Appropriate analyses methods for various types of time series without the need for their editing

Properties of one time series	**Appropriate analyses**
Equally spaced, equally weighted, stationary	LSSA, Fourier transform, wavelet transform, WWZ, LSWA
Equally spaced, equally weighted, non-stationary	Wavelet transform, WWZ, LSWA
Unequally spaced and/or unequally weighted, non-stationary	WWZ, LSWA
Properties of two or more time series	**Appropriate analyses**
Same sampling rates, equally spaced, equally weighted, stationary	LSCSA, XWT, LSCWA
Same sampling rates, equally spaced, equally weighted, non-stationary	XWT, LSCWA
Different sampling rates, equally/unequally spaced, equally/unequally weighted, stationary	LSCSA, LSCWA
Different sampling rates, equally/unequally spaced, equally/unequally weighted, non-stationary	LSCWA

additional samples considered in the least-squares fit (the size of the windows increases by L_0) to achieve the desired time and frequency resolution in the LSWS.

For each k, $1 \le k \le \kappa$, and each j, $1 \le j \le n$, if $1 \le i + j - (L(\omega_k)+1)/2 \le n$, then the size of $\mathbf{y}$ in Eq. (1) (the same as the number of rows in $\mathbf{\Phi}$ in Eq. (2)) is $R(j,k) :=$

$$\begin{cases} \frac{1}{2}\big(L(\omega_k)-1\big)+j, & \text{if } 1 \le j < \frac{1}{2}\big(L(\omega_k)+1\big), \\ L(\omega_k), & \text{if } \frac{1}{2}\big(L(\omega_k)+1\big) \le j \le n - \frac{1}{2}\big(L(\omega_k)-1\big), \\ \frac{1}{2}\big(L(\omega_k)+1\big)+n-j, & \text{if } n - \frac{1}{2}\big(L(\omega_k)-1\big) < j \le n, \end{cases} \tag{4}$$

which is the size of the window located at t_j. Note that when $L_1 = 0$, $L(\omega_k)$ and consequently $R(j,k)$ are independent from the choice of ω_k.

Assume that $\mathbf{P} = \mathbf{C}_{\mathbf{f}}^{-1}$ is the weight matrix associated with $\mathbf{f}$. Let $\mathbf{P_y}$ be the principal submatrix of $\mathbf{P}$ of dimension $R(j,k)$ which is a positive definite matrix. Note that when $\mathbf{P}$ is fully populated, the correlations between data points of the entire time series are considered in each $\mathbf{P_y}$.

If $\mathbf{f}$ contains constituents $\phi_1, \ldots, \phi_q$ of known forms but of unknown amplitudes (e.g., trends or sinusoids of constant frequencies), then for each (t_j, ω_k), let

$$\underline{\mathbf{\Phi}} = \Big[\phi_1\big(t_{i+j-\frac{1}{2}(L(\omega_k)+1)}\big), \ldots, \phi_q\big(t_{i+j-\frac{1}{2}(L(\omega_k)+1)}\big)\Big], \tag{5}$$

$$\overline{\mathbf{\Phi}} = \big[\underline{\mathbf{\Phi}}, \mathbf{\Phi}\big], \tag{6}$$

where $\mathbf{\Phi}$ is given by Eq. (2). Note that $\overline{\mathbf{\Phi}}$ is the new design matrix of order $R(j,k) \times (q+2)$.

A practical approach in the LSWA is to first remove (suppress) the known constituents from each segment of $\mathbf{f}$, and then analyze the residual segment $\hat{\mathbf{g}}$ of $\mathbf{f}$. More precisely, use the model $\mathbf{y} = \underline{\mathbf{\Phi}}\ \underline{\mathbf{c}}$ to estimate $\underline{\mathbf{c}}$ as

$$\hat{\underline{\mathbf{c}}} = \underline{\mathbf{N}}^{-1}\underline{\mathbf{\Phi}}^{\mathrm{T}}\mathbf{P_y}\mathbf{y}, \tag{7}$$

where $\underline{\mathbf{N}} = \underline{\mathbf{\Phi}}^{\mathrm{T}}\mathbf{P_y}\underline{\mathbf{\Phi}}$, and so $\hat{\mathbf{g}} = \mathbf{y} - \underline{\mathbf{\Phi}}\ \hat{\underline{\mathbf{c}}}$. Then use the model $\mathbf{y} = \overline{\mathbf{\Phi}}\ \overline{\mathbf{c}} = \underline{\mathbf{\Phi}}\ \underline{\mathbf{c}} + \mathbf{\Phi}\ \mathbf{c}$ to estimate $\mathbf{c}$ as

$$\hat{\mathbf{c}} = \mathbf{N}^{-1}\mathbf{\Phi}^{\mathrm{T}}\mathbf{P_y}\hat{\mathbf{g}}, \tag{8}$$

where $\mathbf{N} = \mathbf{\Phi}^{\mathrm{T}}\mathbf{P_y}\mathbf{\Phi} - \mathbf{\Phi}^{\mathrm{T}}\mathbf{P_y}\underline{\mathbf{\Phi}}\ \underline{\mathbf{N}}^{-1}\underline{\mathbf{\Phi}}^{\mathrm{T}}\mathbf{P_y}\mathbf{\Phi}$ as discussed in Ghaderpour and Pagiatakis (2017). Note that $\mathbf{c}$ and $\underline{\mathbf{c}}$ are column vectors of dimensions 2 and q, respectively, and $\overline{\mathbf{c}}$ is a column vector of dimension $q+2$ defined as

$$\overline{\mathbf{c}} = \begin{bmatrix} \underline{\mathbf{c}} \\ \mathbf{c} \end{bmatrix}. \tag{9}$$

Let $\mathbf{J} = \mathbf{\Phi}\mathbf{N}^{-1}\mathbf{\Phi}^{\mathrm{T}}\mathbf{P_y}$. The LSWS is defined as

$$s(t_j, \omega_k) = \frac{\hat{\mathbf{g}}^{\mathrm{T}}\mathbf{P_y}\mathbf{J}\hat{\mathbf{g}}}{\hat{\mathbf{g}}^{\mathrm{T}}\mathbf{P_y}\hat{\mathbf{g}}} \in (0,1), \tag{10}$$

where $1 \le j \le n$ and $1 \le k \le \kappa$. Note that $\mathbf{y}$ corresponds to the segment of time series which consists of different constituents, and $\hat{\mathbf{g}}$ represents the constituents of interest (signal) estimated by the least-squares method.

We emphasize that using $\mathbf{y} = \overline{\mathbf{\Phi}}\ \overline{\mathbf{c}} = \underline{\mathbf{\Phi}}\ \underline{\mathbf{c}} + \mathbf{\Phi}\ \mathbf{c}$ to estimate $\mathbf{c}$ considers the correlation among the constituents of known forms and the sinusoidal base functions of cyclic frequency ω_k. Using an alternative model like $\hat{\mathbf{g}} = \mathbf{\Phi}\ \mathbf{c}$ to estimate $\mathbf{c}$ ignores this correlation and may have significant impact on the location of the spectral peaks in the spectrum or spectrogram (Craymer 1998; Ghaderpour and Pagiatakis 2017).

Foster (1996) and Ghaderpour and Pagiatakis (2017) recommend to always consider at least the column of ones, $[\mathbf{1}]$, in $\underline{\mathbf{\Phi}}$ to make the mean values of the segments approximately zero, especially for unequally spaced time series, because the sinusoidal base functions have zero mean. Omitting the column of ones causes poor fitting of the sinusoidal base functions and a false determination of the location of the spectral peak.

Foster (1996) and Ghaderpour and Pagiatakis (2017) have also shown that when $\mathbf{P_y}$ is considered as a vector whose values are Gaussian function values, the sinusoidal base functions will be adapted to Morlet wavelet in the least-squares sense. Other choices for the covariance matrix may adapt the sinusoidal base functions to other type of wavelets in the least-squares sense, one of the reasons why the proposed approach carries the word wavelet.

Appropriate selection of window size parameters L_0 and L_1 in Eq. (3) is crucial in the LSWA. If $L_1 > 0$, then the LSWA inherits similar time and frequency resolutions as the continuous wavelet transform (Mallat 1999), and the frequency resolution increases in the spectrogram as L_0 increases (Ghaderpour and Pagiatakis 2017). Therefore, depending on the scope of analysis and also on the number of constituents of known forms being estimated and removed from the time series, one may empirically choose appropriate values for these parameters.

One may let $R(j,k) = n$ and $j = (n+1)/2$, n odd, in Eq. (10) to obtain the least-squares spectrum (LSS) of the time series of n data points. In fact, the LSS is a special case of the LSWS that is independent of time and has only one segment (the entire time series). The reader is referred to Wells et al. (1985), Pagiatakis (1999) and Ghaderpour and Pagiatakis (2017) for more details.

3 Least-squares cross wavelet analysis

In this section, the cross-spectrogram of two time series (may be extended to more) with its stochastic surfaces at a certain confidence level (usually 95% or 99%) is introduced as well as the phase differences of common constituents of the two time series.

3.1 Cross-spectrogram and its stochastic surface

A random variable X has the beta distribution with parameters $p_1 > 0$ and $p_2 > 0$ on interval $(0,1)$, denoted by β_{p_1,p_2}, if its probability density has the form

$$f_X(x) = \frac{1}{B(p_1,p_2)} x^{p_1-1}(1-x)^{p_2-1}, \tag{11}$$

where $B(p_1,p_2) = \Gamma(p_1)\Gamma(p_2)/\Gamma(p_1+p_2)$, and Γ is the Gamma function (e.g., Gupta 2004; Craig et al. 2013).

It is shown in Ghaderpour and Pagiatakis (2017) that the LSWS of time series $\mathbf{f}$ given by Eq. (10) follows the beta distribution, in other words, $s \sim \beta_{1,\Re/2}$, where β stands for the beta distribution, $\Re = R(j,k) - q - 2$, and the symbol $\sim$ is used to show that a random variable follows a distribution.

Suppose that time series $\mathbf{f_1}$ and $\mathbf{f_2}$ have been derived from two statistically independent populations of random variables following respectively the multidimensional normal distributions $\mathcal{N}(\mathbf{0}, \mathbf{C_{f_1}})$ and $\mathcal{N}(\mathbf{0}, \mathbf{C_{f_2}})$, where the covariance matrices $\mathbf{C_{f_1}}$ and $\mathbf{C_{f_2}}$ may be singular. Let $\mathbf{\Omega} = \{\omega_k;\ k = 1, \ldots, \kappa\}$ be a set of common spectral frequencies for the two time series under consideration.

Let s_1 and s_2 be the spectrograms corresponding to $\mathbf{f_1}$ and $\mathbf{f_2}$, respectively. By the assumption, s_1 and s_2 are statistically independent. For each pair (t_j, ω_k), denote by X_s the cross-spectrogram of the two time series and define it as the product of their spectrograms,

$$X_s = s_1 s_2. \tag{12}$$

Note that $0 < X_s < 1$ because $0 < s_1, s_2 < 1$. Since the sampling rates and/or the times of the two time series may not be the same, one may set the time vector in X_s as the union of the sets of times of the first and second time series. If t_j is a time in the first time series but not in the second (or vice-versa), then $s_1(t_j, \omega_k)$ is calculated within a window of size $R_1(j,k)$ located at t_j, and $s_2(t_j, \omega_k)$ is calculated within a window of size $R_2(j,k)$ located at t_j, emphasizing that the center of the window does not have to be located at a time in which there exists a sample. For a pair (t_j, ω_k), if the value of X_s is closer to one, then the two segments of the two time series within the windows of sizes $R_1(j,k)$ and $R_2(j,k)$ are highly coherent, and they are highly incoherent if the value of X_s is closer to zero.

Suppose that q_1 and q_2 are the number of constituents of known forms being considered in the calculation of the spectrograms for $\mathbf{f_1}$ and $\mathbf{f_2}$, respectively. Ghaderpour and Pagiatakis (2017) showed that $s_1 \sim \beta_{1,\Re_1/2}$ and $s_2 \sim \beta_{1,\Re_2/2}$, where $\Re_1 = R_1(j,k) - q_1 - 2$ and $\Re_2 = R_2(j,k) - q_2 - 2$. More precisely, from Eq. (11), the probability distribution functions (PDF) of the independent random variables s_1 and s_2 are respectively as follows

$$f_{s_1}(u) = \frac{\Re_1}{2}(1-u)^{\Re_1/2-1}, \qquad 0 < u < 1, \tag{13}$$

$$f_{s_2}(v) = \frac{\Re_2}{2}(1-v)^{\Re_2/2-1}, \qquad 0 < v < 1. \tag{14}$$

Following similar methodologies in Glen et al. (2004), the PDF of random variable X_s can be obtained. The following transformation is a one-to-one mapping from $A = \{(u,v);\ \ 0<u<1,\ 0<v<1\}$ to $B = \{(x,y);\ \ 0<x<1,\ 0<y<1\}$

$$X_s = s_1 s_2, \qquad Y = s_2. \tag{15}$$

Let T and K denote the transformation and the inverse transformation, respectively. Therefore,

$$\begin{aligned} x &= T_1(u,v) = uv, & y &= T_2(u,v) = v,\\ u &= K_1(x,y) = x/y, & v &= K_2(x,y) = y. \end{aligned} \tag{16}$$

The Jacobian of the transformation is

$$\begin{aligned} J = \frac{\partial(u,v)}{\partial(x,y)} &= \Big(\frac{\partial u}{\partial x}\Big)\Big(\frac{\partial v}{\partial y}\Big) - \Big(\frac{\partial u}{\partial y}\Big)\Big(\frac{\partial v}{\partial x}\Big)\\ &= \Big(\frac{1}{y}\Big)(1) - \Big(\frac{-x}{y^2}\Big)(0) = \frac{1}{y}. \end{aligned} \tag{17}$$

Using Eq. (16) and the independency of s_1 and s_2,

$$f_{X_s,Y}(x,y) = |J| f_{s_1,s_2}(u,v) = \frac{1}{y} f_{s_1}(x/y) f_{s_2}(y). \tag{18}$$

Integration of Eq. (18) with respect to y over the appropriate interval and using Eqs. (13) and (14) yield the PDF of X_s

$$\begin{aligned} f_{X_s}(x) &= \int_x^1 f_{X_s,Y}(x,y)\,dy = \int_x^1 \frac{1}{y} f_{s_1}\Big(\frac{x}{y}\Big) f_{s_2}(y)\,dy\\ &= \frac{\Re_1\Re_2}{4}\int_x^1 \frac{1}{y}\Big(1-\frac{x}{y}\Big)^{\Re_1/2-1}(1-y)^{\Re_2/2-1}\,dy, \end{aligned} \tag{19}$$

where $0 < x < 1$. One may numerically calculate this integral using the well-known methods such as Simpson quadrature and Gauss-Kronrod quadrature (Hazewinkel 2001; Moler 2008; Shampine 2008). Figure 1 shows the PDF of X_s for selected values of $\Re_1$ and $\Re_2$.

Table 2 shows the critical values (cv) corresponding to two significance levels $\alpha = 0.01$ and $\alpha = 0.05$ for selected values of $\Re_1$ and $\Re_2$. It can be seen that the critical values approach zero rapidly when $\Re_1$ and $\Re_2$ increase. Note that the area under the density curve from its lower right tail to the left is computed to find the critical value for a certain significance level because the PDF becomes singular when approaching zero.

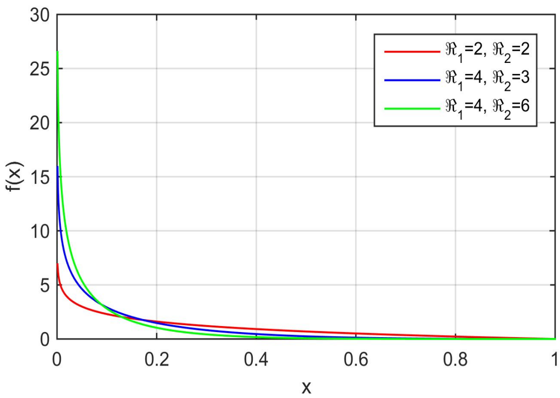

Fig. 1 Illustration of the PDF of X_s given by Eq. (19) for some values of $\Re_1$ and $\Re_2$

Table 2 The critical values (cv) corresponding to the significance levels (α) and $\Re_i$

$\Re_1$	$\Re_2$	$\alpha = 0.01$	$\alpha = 0.05$
2	2	$cv = 0.862$	$cv = 0.701$
4	3	$cv = 0.624$	$cv = 0.436$
4	6	$cv = 0.452$	$cv = 0.290$
10	10	$cv = 0.186$	$cv = 0.105$
20	30	$cv = 0.043$	$cv = 0.022$
100	101	$cv = 0.003$	$cv = 0.002$

Now let $\mathbf{f_1}$ and $\mathbf{f_2}$ be two time series of dimensions n_1 and n_2, respectively. For each $\omega_k \in \mathbf{\Omega}$, assume that s_1 and s_2 are the least-squares spectra corresponding to $\mathbf{f_1}$ and $\mathbf{f_2}$, respectively. Analogous to the cross-spectrogram, define the least-squares cross spectrum (LSCS) as $X_s = s_1 s_2$, where $\Re_1 = n_1 - q_1 - 2$ and $\Re_2 = n_2 - q_2 - 2$. The PDF of X_s is given by Eq. (19). Note that the LSCS is independent of the sampling rates because it decomposes the time series to the frequency domain and not to the time-frequency domain.

3.2 Phase differences in the cross-spectrogram

When analyzing two time series together, researchers are also interested in the phase differences between any two constituents of interest of the same time-frequency spectral value. To find the phase differences, note that

$$\begin{aligned} \mathbf{y} &= a\sin\,(2\pi\omega\mathbf{t} + \theta)\\ &= \big[\cos\,(2\pi\omega\mathbf{t}),\ \sin\,(2\pi\omega\mathbf{t})\big]\mathbf{c} = \mathbf{\Phi c}, \end{aligned} \tag{20}$$

where $\mathbf{c} = a\,\big[\sin\theta,\ \cos\theta\big]^{\mathrm{T}}$ and $\mathbf{\Phi}$ is the design matrix given by Eq. (2). Following the same procedure in the LSWA, one can see that Eq. (8) is the estimate for $\mathbf{c}$. For each pair (t_j, ω_k), let $\hat{c}_1$ and $\hat{c}_2$ be the two elements of

$\hat{\mathbf{c}}$ given by Eq. (8). Therefore, $\hat{a}\sin\hat{\theta} = \hat{c}_1$ and $\hat{a}\cos\hat{\theta} = \hat{c}_2$, and so $\hat{a} = (\hat{c}_1^2 + \hat{c}_2^2)^{0.5}$. Thus

$$\hat{\theta} = 2\arctan\left(\frac{1-\hat{c}_2/\hat{a}}{\hat{c}_1/\hat{a}}\right). \tag{21}$$

Now for pair (t_j, ω_k), if $\hat{\theta}_1$ and $\hat{\theta}_2$ are the phase differences of the constituents of $\mathbf{f_1}$ and $\mathbf{f_2}$ calculated by Eq. (21), respectively, then define the phase difference corresponding to pair (t_j, ω_k) as $\psi = \hat{\theta}_2 - \hat{\theta}_1$, where $-2\pi < \psi < 2\pi$. The phase difference for a common constituent of a particular frequency indicates how much the constituent of the second time series lags (if $-2\pi < \psi < -\pi$ or $0 \le \psi < \pi$) or leads (if $-\pi \le \psi < 0$ or $\pi \le \psi < 2\pi$) the constituent of the first time series. Let σ_1^2 and σ_2^2 be the variances associated with $\hat{\theta}_1$ and $\hat{\theta}_2$, respectively, estimated from the least-squares estimation process. Applying the covariance law to $\psi = \hat{\theta}_2 - \hat{\theta}_1$, one may calculate the standard deviation of ψ as $\sigma_\psi = \left(\sigma_1^2 + \sigma_2^2\right)^{0.5}$.

4 Analysis of two synthetic time series

We demonstrate the performance of the LSCSA and LSCWA on two synthetic and inherently unequally spaced time series given by

$$f_1(t_i) = \cos\left(\frac{30}{1.2 - t_i}\right) + g(t_i) + w_1, \tag{22}$$
$$0 \le t_i \le 1,\ 1 \le i \le 600,$$

where $g(t_i) = \cos\left(25 \cdot 2\pi t_i\right)$ for $200 \le i \le 300$ and $g(t_i) = 0$, otherwise, and w_1 is Gaussian white random noise, and

$$f_2(t'_j) = \cos\left(5 \cdot 2\pi t'_j\right) + \cos\left(25 \cdot 2\pi t'_j + \frac{\pi}{2}\right) + w_2, \tag{23}$$
$$0 \le t'_j \le 1,\ 1 \le j \le 400,$$

where w_2 is Gaussian white random noise. Note that in the LSSA, LSWA, LSCSA, and LSCWA, the time series do not have to contain white noise. In this example, we consider white noise to see the performance of these analyses because measurements in practice typically contain white noise. Time series $\mathbf{f_1} = [f_1(t_i)]$ and $\mathbf{f_2} = [f_2(t'_j)]$ are illustrated in Fig. 2a with blue and red colors, respectively. Assume that the unit time for $\mathbf{f_1}$ and $\mathbf{f_2}$ is in days. The set of common frequencies chosen in the analyses of the two time series is $\mathbf{\Omega} = \{1, 2, \ldots, 49\}$ cycles per day (c/d).

The LSCS of the two time series detects two peaks at cyclic frequencies 5 and 25 c/d (Fig. 2b). Figure 2b also shows the phase differences of the constituents of cyclic frequencies 5 and 25 c/d in $\mathbf{f_1}$ with respect to the ones in $\mathbf{f_2}$ which are approximately close to $-50°$ and $+90°$, respectively, as expected from the synthetic time series. In the next step, the peak at 5 c/d is suppressed and the LSCS of the residual time series is shown in Fig. 2c. It can be seen that the percentage variance of the peak at 25 c/d increases, indicating more coherency in the residual time series.

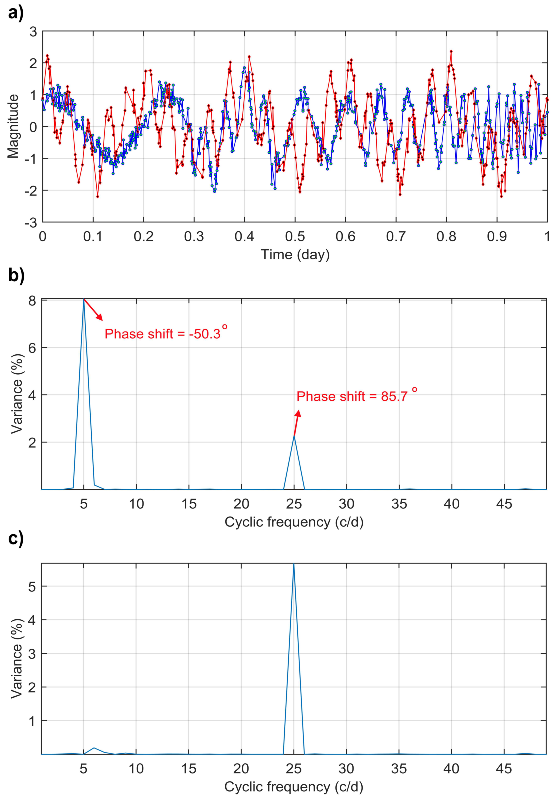

Fig. 2 (a) Two unequally spaced series given by Eqs. (22) and (23) shown in blue and red, respectively, (b) The LSCS of the two time series and (c) The LSCS of the two residual time series after suppressing the peak at 5 c/d

Since there are 600 and 400 samples per day for $\mathbf{f_1}$ and $\mathbf{f_2}$, respectively, $M_1 = 600$ and $M_2 = 400$. Note that since the time series are inherently unequally spaced, no aliasing is expected to occur at high frequencies, however, if at least one of the time series was equally spaced, then it is recommended to choose half of the sampling rate as the Nyquist frequency for the cross-spectrogram. The cross-spectrograms of the two time series and their residuals along with some selected phase differences (arrows) are shown in Fig. 3 ($L_1 = 2$ and $L_0 = 10$ are selected for both time series). The angles of white arrows on the cross-spectrogram with respect to the horizontal axis show the phase differences. Note that an arrow is in the first or second quadrant of the trigonometric circle when $0° \le \psi < 180°$, and it is in the third or fourth quadrant when $-180° \le \psi < 0°$.

The coherency of the two original time series can be observed in more details in Fig. 3a. The cross-

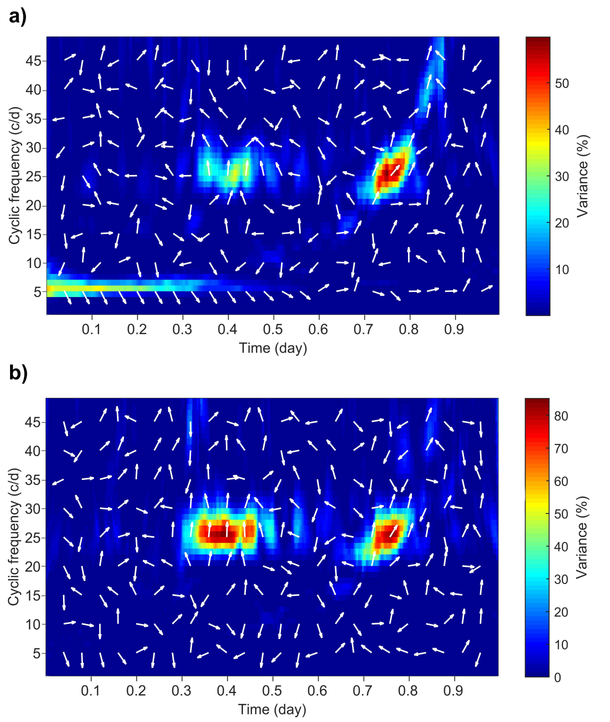

Fig. 3 (a) The LSCWS of the time series shown in Fig. 2a and (b) The LSCWS of the residual time series. The arrows in the spectrogram show the phase differences

spectrogram shows that the hyperbolic chirp signal in Eq. (22) is coherent with the cosine wave of 5 c/d in Eq. (23) from 0 to 0.5 day interval. The percentage variance of the corresponding peaks decreases as time increases because the frequencies of the hyperbolic chirp in $\mathbf{f_1}$ increases rapidly over time, showing less coherency with the cosine wave of 5 c/d in $\mathbf{f_2}$ as time increases. It can be seen from Fig. 3a that signal $g(t_i)$ in $\mathbf{f_1}$ and the cosine wave of 25 c/d in $\mathbf{f_2}$ are coherent in the time period of approximately $0.3 - 0.5$ day. Part of the hyperbolic chirp at 25 c/d in $\mathbf{f_1}$ and the cosine wave of 25 c/d in $\mathbf{f_2}$ are also coherent in the time period of approximately $0.7 - 0.8$ day. Figure 3b is obtained by suppressing (removing) the peaks at 5 c/d in the LSCWS that can be done by adding the sine and cosine base functions of 5 c/d as two columns to $\underline{\mathbf{\Phi}}$ in Eq. (5) for $\mathbf{f_2}$. The coherency between signal $g(t_i)$ in $\mathbf{f_1}$ and the cosine wave of 25 c/d in the residual $\mathbf{f_2}$ is significantly increased (compare the percentage variance of the peaks in Fig. 3a and b from time 0.3 to 0.5 day at 25 c/d).

The phase difference of almost 90° can be observed in the spectrogram from time 0.35 to 0.5 day at 25 c/d as expected. Note that the phase differences in the LSCS may not be accurate for non-stationary time series as the sinusoids are being fitted to the entire time series. For instance, the phase difference in the LSCWS corresponding to time 0.77 d and frequency 25 c/d is 43.2°, but it cannot be detected as such in the LSCS. Moreover, the coherency between signal $g(t_i)$ in $\mathbf{f_1}$ and cosine wave of frequency 25 c/d in $\mathbf{f_2}$ is more localized and significant in Fig. 3b.

5 GOCE electrostatic gravity gradiometer measurements and Poynting energy flux

Two different geophysical time series are analyzed to demonstrate the performance of LSCWA when is applied to real, unequally spaced and unequally weighted time series. The first time series is composed of gravitational gradient disturbances observed by GOCE satellite, whereas the second time series comprises Poynting electromagnetic energy flux (plasma flow) in the ionosphere derived from equivalent horizontal ionospheric currents and vertical currents. The hypothesis of this analysis is that the electromagnetic energy flux in the Earth's thermosphere introduces undesirable disturbances in GOCE electrostatic gravity gradiometer (EGG) measurements as shown in Ince (2016) and Ince and Pagiatakis (2016). The data sets are described and their analyses are presented in this section.

5.1 GOCE electrostatic gravity gradiometer

The latest gravity field mission GOCE was one of the three satellite missions, after CHAMP (challenging mini-satellite payload) and GRACE (gravity recovery and climate experiment), which has helped remarkably to improve the accuracy and resolution of the Earth's global geopotential models from space. In order to map the Earth's gravitational field from satellite measurements, the influence of all temporal gravitational and non-gravitational accelerations acting on the satellite should be measured and removed from the observations.

Preliminary analyses and literature search have shown that the GOCE electrostatic gravity gradiometer (EGG) measurements (Rummel et al. 2011) are affected by some unknown non-gravitational sources around the magnetic poles (Peterseim et al. 2011; Stummer et al. 2012; Siemes et al. 2012; Yi et al. 2013; Ince 2016; Ince and Pagiatakis 2016). Ince (2016) demonstrated that the source of these disturbances are related to solar activity dependent ionospheric dynamics. Moreover, these disturbances can reach up to a magnitude of about 3 to 5 times larger than the expected noise level (approximately 11 milli-Eotvos, mE) of the gravity field components at specific epochs. Ince and Pagiatakis (2016) found that these specific epochs correspond to geomagnetic storms due to the interaction between the interplanetary magnetic field and geomagnetic field.

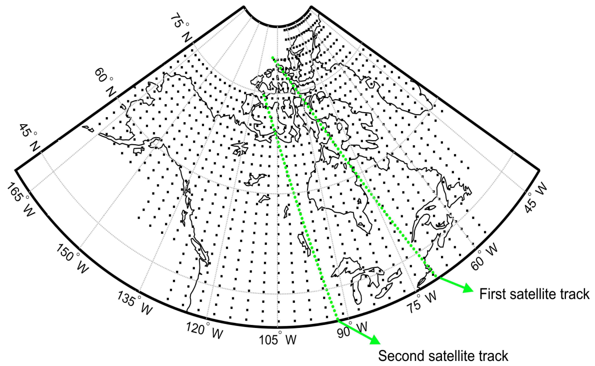

Fig. 4 Two satellite ascending tracks (green curves) over Canada. The grid points represent the SEC grid

In order to understand the relation between the undesirable disturbances observed in gravitational gradients and plasma flow variations due to solar activity, spherical elementary currents (SEC) are used for the coherency analysis (Amm 1997; Amm and Viljanen 1999; Weygand et al. 2011). Based on the Laplace condition, the summation of the diagonal components of the gravitational gradient tensor (GGT) (trace) should be zero. It is worth mentioning that these variations affect the EGG measurements around the auroral oval when the ionospheric dynamics (plasma flow) are more intense. In this example, the trace on which these spurious signals are more visible is investigated, and the selected GOCE tracks are examined individually in which the trace is subject to rapid changes (Fig. 4).

The sampling period of GOCE measurements is one sample per second, and along track correlated errors are not considered in this study (error in the GOCE gradients outside of the measurement bandwidth is colored). The data sets we analyze do not have any gaps and they are equally spaced. However, it is possible that GOCE data in level zero or level one stage have gaps.

5.2 Equivalent ionospheric currents and Poynting vector

The SEC system (SECS) methodology given in Amm (1997) and Amm and Viljanen (1999) are used to derive equivalent ionospheric currents (EIC) which are based on the magnetic field disturbances measured at the Earth's surface (Weygand et al. 2011). The SECS methodology furthermore upward continues the anomalous magnetic field measurements from the ground to an altitude of about 110 km. Equivalent currents (horizontal currents) and spherical elementary current amplitudes (vertical currents) are provided in 10 s temporal resolution in a gridded format over North America and West Greenland (see the grid points in Fig. 4). The kriging method (using a variogram) is applied to interpolate the grid values into the satellite ground track position (see green lines in Fig. 4) for the analyses (Ince 2016).

By using SEC values provided on a grid (see dots in Fig. 4) interpolated into the satellite position, the Poynting vector (Kelley 2009; Ince 2016) is computed in the north-south and east-west directions along the satellite track. The units of Poynting vector are Watt per meter square (W/m^2). In general, the direction of the Poynting vector indicates the direction of the flow of the electromagnetic energy that drives the ionospheric currents.

The gravitational gradient tensor (GGT) trace and the Poynting vector (series) of the first satellite track are shown in Fig. 5a. The unit time for our analyses is in hours and the sampling rate for original GGT trace series is $M_1 = 3600$ samples per hour. The sampling rate for the Poynting series is $M_2 = 360$ samples per hour. Note that the Nyquist frequency of the Poynting series is 180 cycles per hour (c/h) which is different from the one for the original GGT trace series of 1800 c/h. Therefore, the maximum frequency for the analysis must not be greater than 180 c/h. In this analysis, we choose $\boldsymbol{\Omega} = \{1, 2, \ldots, 100\}$. The LSCS after removing the datum shift of the original GGT trace series is shown in Fig. 5b. The original GGT trace and the Poynting series of the second satellite track and their LSCS (after removing the datum shift) are also shown in Fig. 6.

Note that the XWT (Grinsted et al. 2004) would require interfiling and editing of both time series to be identical in their times and equally spaced, and it does not consider the covariance matrices associated with the time series. However, the LSCWA does not require the series to have the same sampling rates and to be equally spaced at identical times. The comparison between the XWT and LSCWA for equally spaced time series of the same sampling rates are shown below. This comparison is made only for the first satellite track.

In order to apply the XWT, the GGT trace series of the first satellite track should be decimated from 3600 to 360 samples per hour ($M_1 = 360$) because the Poynting series has the sampling rate of 360 samples per hour. To keep the useful information of the GGT trace series as much as possible, a Gaussian filter is used in this process (see Appendix 1). The result of the decimated GGT trace series is illustrated in black in Fig. 5a, and it can be observed that the decimated data points match the data points of Poynting series in time.

Figure 7 shows the XWT of the decimated GGT trace series and the Poynting series of the first satellite track (the Morlet wavelet is used). The MATLAB

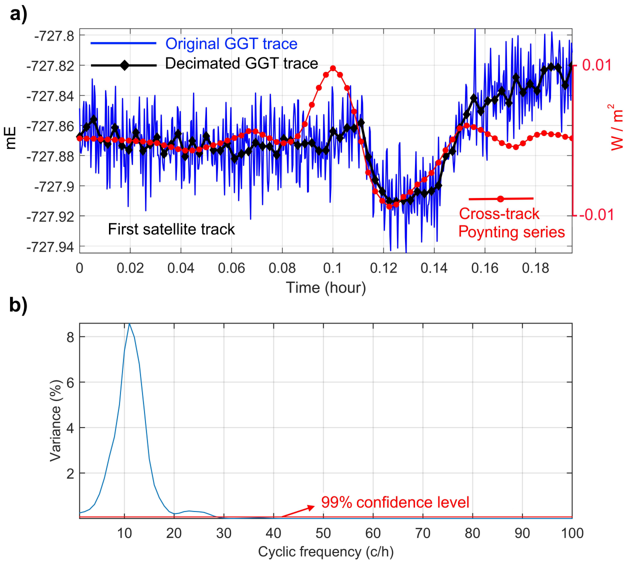

Fig. 5 (a) The cross-track Poynting vector component in W/m^2, original and decimated GGT trace series in mE for the first satellite track, and (b) The LSCS of original GGT trace and cross-track Poynting vector component series with 99% confidence level

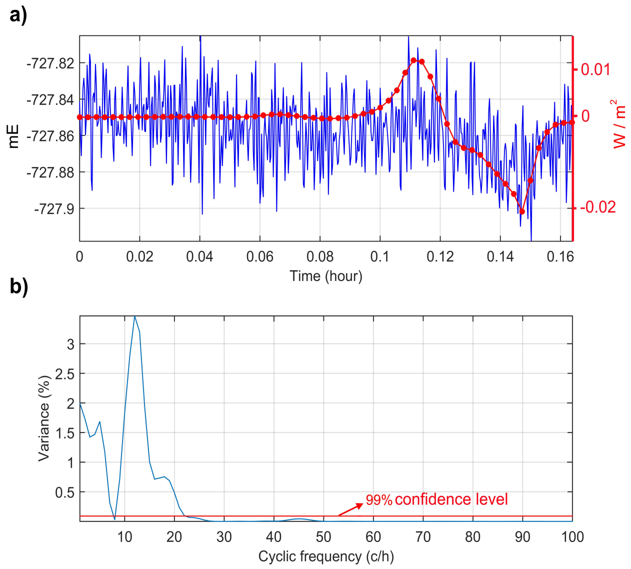

Fig. 6 (a) The original GGT trace series shown by blue and the cross-track Poynting vector component series shown in red for the second satellite track, and (b) The LSCS of the original GGT trace and cross-track Poynting vector component series with 99% confidence level

code to generate this figure was obtained from www.mathworks.com/matlabcentral/fileexchange/ 47985-cross-wavelet-and-wavelet-coherence. Note that the XWT is in time-scale, and the scales are converted to frequencies in this figure. The confidence level $Z_2(p)$ associated with a probability p in the XWT may be

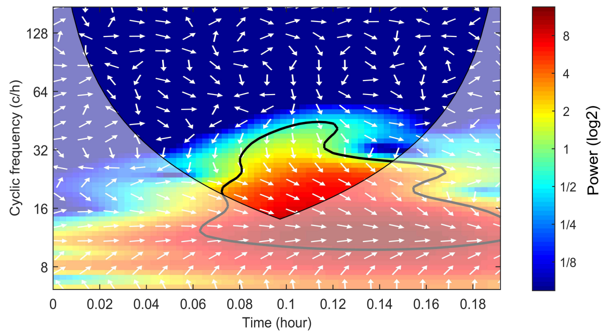

Fig. 7 The XWT of the decimated GGT trace and Poynting series of the first satellite track along with phase shifts (arrows). The area within the thick contour is the significant area at 99% confidence level. The cone of influence where the edge effects might distort the results is shown as a light shade

calculated by inverting the following integral

$$p = \int_0^{Z_2(p)} z \; K_0(z) \; dz, \tag{24}$$

where $K_0(z)$ is the modified Bessel function of order zero (Torrence and Compo 1998; Ge 2008). From Eq. (24), one can obtain $Z_2(0.95) = 3.999$ and $Z_2(0.99) = 5.767$. The latter value is used in Fig. 7.

The LSCWA for the first satellite track is applied to three different cases, namely, the decimated GGT without (as in the XWT above) and with considering the covariance matrix and the original GGT trace series. Based on the constituents of low frequency and short duration empirically observed in the time series, the window size parameters are chosen as $L_1 = 1$ and $L_0 = 5$ for both time series and $\underline{\mathbf{\Phi}} = [\mathbf{1}]$ for the decimated GGT trace series to remove its datum shifts.

Figure 8a shows the LSCWS of the decimated GGT trace series by considering the covariance matrix generated by the Gaussian filtering process described in Appendix 1. The significant peaks in the LSCWS are those that are above the stochastic surface shown by gray at 99% confidence level. The two-dimensional representation of the LSCWS and its stochastic surface (gray) and phase differences are shown in Fig. 8b. It can be seen that the two time series are highly coherent with approximately zero phase differences (see the reddish area around 0.12 hour in Fig. 8b). This fact can also be observed in Fig. 7. The very low coherence in the interval $0.02 - 0.1$ hours is also expected due to the lower power random character of the signals (Fig. 5a). However, the significant peaks are much more localized in the LSCWS than in the XWT because the LSCWS is obtained from the spectrograms, decomposing the time series directly to the time-frequency domain using the least-squares method. Although the Morlet wavelet

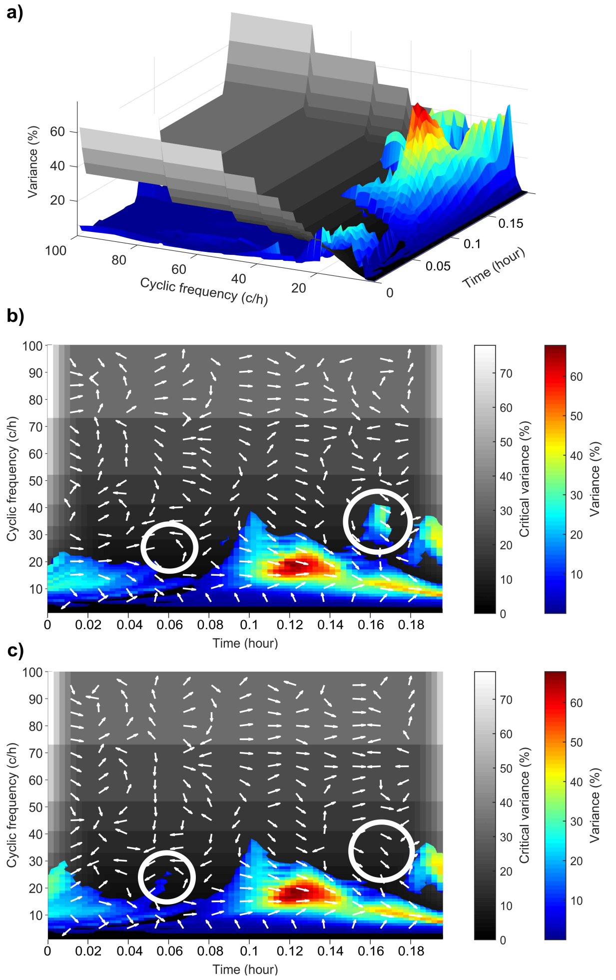

Fig. 8 (a) Three-dimensional representation of the LSCWS of the Poynting and decimated GGT trace series shown in Fig. 5a considering the covariance matrix with the stochastic surface at 99% confidence level (gray), (b) its two-dimensional representation with phase differences (arrows), and (c) The LSCWS without considering the covariance matrix with phase differences (arrows)

used in the XWT smooths the signal peaks in the spectrogram, it increases the bandwidth of the signal frequencies in the spectrogram (poor time-frequency resolution, Ghaderpour and Pagiatakis 2017).

To verify the importance of the covariance matrix in the analysis, an equally weighted analysis without considering the covariance matrix is also performed (Fig. 8c), and some of the cross-spectrogram values (denoted by $X_s(t_j, \omega_k)$) are shown in Table 3 and compared to the values when the covariance matrix is considered (denoted by $X_s^e(t_j, \omega_k)$). In Table 3, $cv(t_j, \omega_k)$ denotes the critical values (%) corresponding to pair (t_j, ω_k) at 99% confidence level. Comparing the values in the third and fourth columns, one can observe the changes in percentage variances for the LSCWS. The first five and last nine rows in this table correspond to some of the values inside the left and right circles, respectively, shown in Fig. 8b and c. Many of the peaks that are significant in Fig. 8b are insignificant in Fig. 8c (inside the right circle). On the other hand, many of the peaks that are insignificant in Fig. 8b are significant in Fig. 8c (inside the left circle).

Table 3 Comparison between some of the values in the LSCWS with (third column) and without (fourth column) considering the covariance matrix associated with the decimated GGT trace series and the critical value (fifth column) at 99% confidence level

t_j	ω_k	$X_s^e(t_j, \omega_k)$	$X_s(t_j, \omega_k)$	$cv(t_j, \omega_k)$
0.058	19	3.82	9.16	5.9
0.058	20	3.84	9.01	5.9
0.058	22	4.37	9.45	7.02
0.061	25	8.03	10.13	8.5
0.061	26	7.45	8.98	8.5
0.153	23	11.73	6.45	7.02
0.158	21	5.94	4.95	5.9
0.158	28	16.36	9.02	10.5
0.164	36	29.4	7.71	13.28
0.164	37	29.32	8.47	13.28
0.167	36	33.99	7.52	13.28
0.167	37	34.22	8.65	13.28
0.169	36	20.72	6.61	13.28
0.169	37	22.49	7.97	13.28

For the original GGT trace series, the same window size parameters are selected but $M_1 = 3600$ (Fig. 9). Since the window size for the original GGT trace series is larger than for the decimated one, the critical values of the LSCWS of the original GGT trace series are smaller than the ones for the decimated GGT trace series (Figs. 8b, 9a). This means that the spectral peaks in the LSCWS for the decimated series are expected to be stronger than the ones for the original series in order to be statistically significant. Comparing Fig. 8b and c with Fig. 9a, one can observe that Fig. 9a is closer to Fig. 8b in terms of significant peaks (e.g., see inside the circles). This indicates the crucial importance of considering the covariance matrix associated with the series when computing the spectrogram (the weighted LSCWA).

The analysis of the original GGT trace series (Fig. 9a) shows that the effects of the marginal windows are improved and more reliable results for the coherency and the phase differences are obtained. We emphasize that various filtering and decimating techniques may alter the result of analysis, and so analyzing the original series (raw data) will give more reliable results. There-

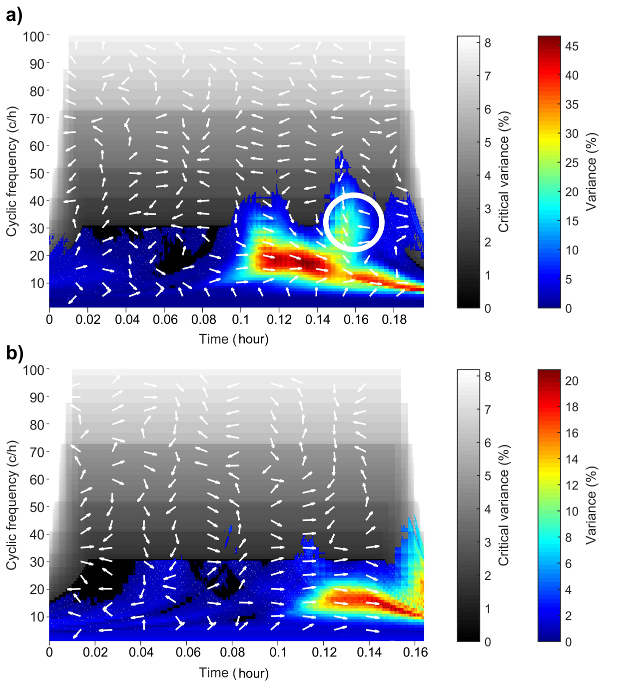

Fig. 9 The LSCWS of the original GGT trace series and the Poynting series with stochastic surface at 99% confidence level (gray) along with the phase differences for (a) the first satellite track and (b) the second satellite track

fore, for the second satellite track, we only illustrate the LSCWS of the original GGT trace and Poynting series (shown in Fig. 6a) in Fig. 9b.

There is a small negative phase difference around cyclic frequency 20 c/h and time $0.12 - 0.14$ h in Fig. 9a and b indicating that the ionospheric variations are leading the disturbances in GGT trace series. The analyses show that the variations observed in the two series have a period of about 5 minutes. This corresponds to spatial variations of around 2000 km. The ionospheric variations of this spatial resolution were investigated and presented in Ince and Pagiatakis (2016).

6 Westford-Wettzell VLBI baseline length and atmospheric temperatures

In this section, the effect of atmospheric temperature on the VLBI baseline length estimates between Westford in the USA and Wettzell in Germany is investigated, and the coherency between the temperature variations at the two stations and the VLBI baseline are shown. The VLBI length series and the associated variances are obtained from www.ccivs.bkg.bund.de, and the temperature time series for Westford and Wettzell are obtained from http://ggosatm.hg.tuwien.ac.at/DELAY/SITE/VLBI/.

The VLBI series comprises 1733 unequally spaced and unequally weighted baseline length estimates from January 9th, 1984 at 19:12:00 universal time (UT) to September 3rd, 2014 at 16:48:00 UT (Fig. 10a). In order to see the effect of the atmospheric temperature on the Westford-Wettzell baseline length, the temperatures are chosen close to, and in many cases identical to the times when the baseline length estimates are available (Fig. 10b). Since there are 57 samples per year (on average), $M = 57$. In order to compare the results with the results in Ghaderpour and Pagiatakis (2017), the window size parameters are chosen as $L_1 = 4$ and $L_0 = 30$, and the set of cyclic frequencies is $\mathbf{\Omega} = \{0.1, 0.2, 0.3, \dots, 12\}$ with unit of cycles per annum (c/a). Selecting smaller window size parameters will produce cross-spectrograms that are more localized in time and more accurate in phase shifts; however, frequency localization will be poorer (see Sect. 4).

The linear trend observed in Fig. 10a expresses the lengthening of the baseline due to the relative tectonic plate movement on which the two VLBI antennas are mounted (Campbell 2004). Therefore, the linear trend is the known constituent, so in Eq. (5), we let $\underline{\mathbf{\Phi}} = [\mathbf{1}, \mathbf{t}]$. Figure 11 shows the (weighted) cross-spectrograms of the VLBI series and each of the temperature series (after removing the trends) along with their stochastic surfaces at 99% confidence level. The coherency between the two series at the cyclic frequency 1 c/a (365 days) can be seen in the figure. From the cross-spectrograms, one can observe that both temperature series show rela-

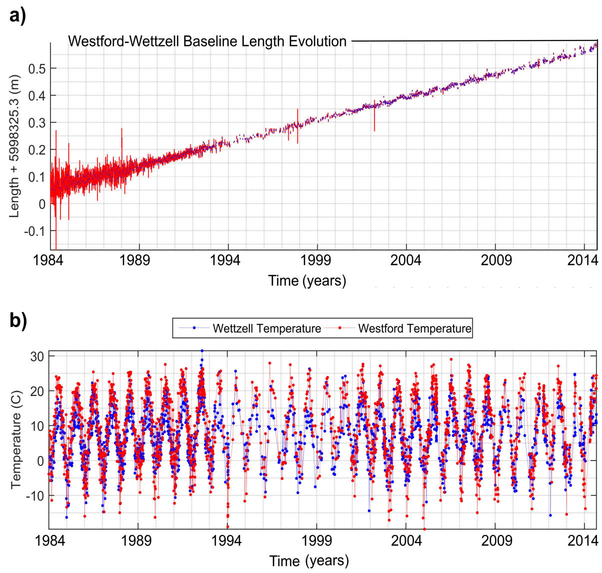

Fig. 10 (a) The unequally spaced VLBI baseline length evolution since January 1984 with error bars (red), and (b) unequally spaced and equally weighted temperature series at stations Westford (red) and Wettzell (blue) since January 1984

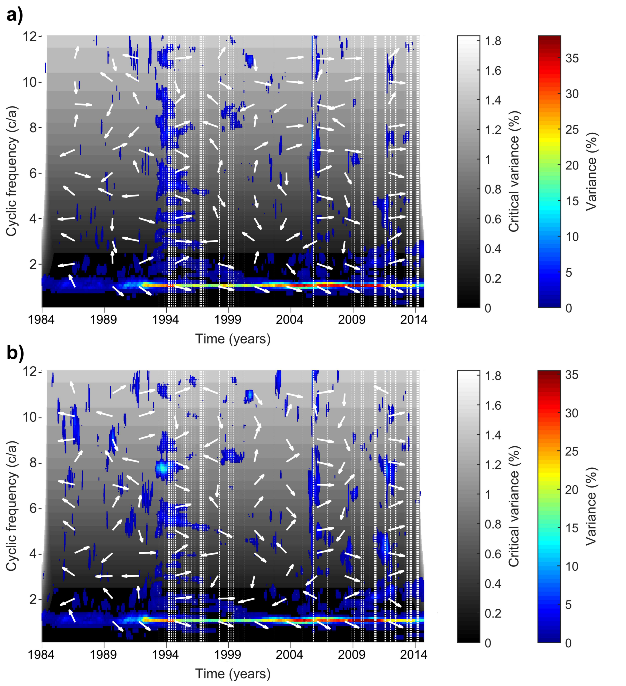

Fig. 11 The LSCWS of the residual VLBI series and the (a) Westford and (b) Wettzell temperature series with their stochastic surfaces at 99% confidence level (gray) and phase differences (white arrows)

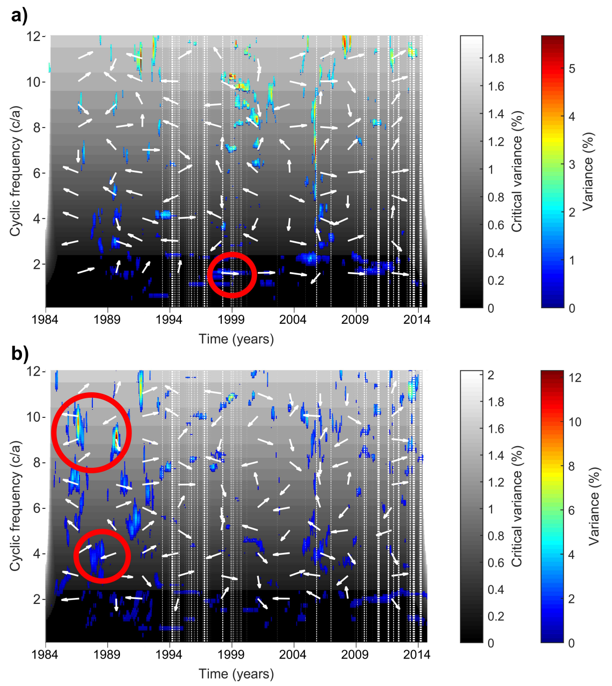

Fig. 12 The LSCWS of the residual VLBI series and the residual (a) Westford and (b) Wettzell temperature series with their stochastic surfaces at 99% confidence level (gray) and phase differences (white arrows). Some of the significant peaks are shown inside the circles

tively small coherency at 1 c/a with the VLBI series for the time period from 1984 to 1991. This small coherency is due to large measurement errors for the VLBI series in that period (Fig. 10a). Ghaderpour and Pagiatakis (2017) show that considering the error bars of the VLBI series improves the percentage variances of the spectral peaks in the LSWS, and it results in improved coherency with the temperature series.

The VLBI series has approximately the same phase shifts over time with both temperature series at 1 c/a (the constituents of the temperature series at 1 c/a have approximately zero phase shifts) indicating simultaneous contraction and expansion at both antennas which results in significant periodic change in the baseline length (see arrows). The small negative phase differences mean that the constituents of each temperature series lead the constituents of VLBI series at period of one year, indicating that the periodic change in the VLBI baseline length slowly occurs after the temperature variation. In other words, depending on the design of the antennas, the annual temperature variation can affect the geometry of the antennas by several millimeters (Wresnik et al. 2007). The constituents of the VLBI series and each temperature series at cyclic frequency 1 c/a have slightly smaller phase differences at certain time periods from 1989 to 2014 when selecting smaller window size parameters (e.g., $L_1 = 1$ and $L_0 = 10$).

For further investigation, the annual peaks are also suppressed from the VLBI baseline length series as well as from the Westford temperature series, and the LSCWS of the residual series is shown in Fig. 12a. The weak peak at 1.6 c/a in Fig. 12a may indicate that the Westford antenna is being deformed with a period of approximately 228 days (unusual atmospheric temperature variations) from year 1997 to year 2001 with almost zero phase shift (see inside the circle) as was discussed in Ghaderpour and Pagiatakis (2017).

To compare the results with the result of Wettzell temperature series shown in Ghaderpour and Pagiatakis (2017), the trends, the annual peaks, and peaks at frequency 1.6 c/a are simultaneously removed from the VLBI series. The trends and annual peaks are also removed from the Wettzell temperature series and the LSCWS of the two residual series is shown in Fig. 12b. The statistically significant coherency between the constituents of the two series in the LSCWS indicates the deformation of Wettzell antenna, possibly affecting the baseline length at certain periods (see inside the circles). The semiannual length variation of the baseline length can be possibly linked to the temperature variation as observed in the cross-spectrograms shown in Fig. 12 (since 2004). The dashed vertical lines in the cross-spectrograms are due to significant data gaps.

7 Discussions and Conclusions

A new method of analyzing two time series together using the LSWA is introduced which is a natural extension of the LSSA. This method, namely, the LSCWA can be applied to any type of time series and generates fairly simple and meaningful results including the confidence level and phase differences between the two time series, and it shows how much the constituents of the time series in a particular frequency are coherent and whether the coherency is significant at certain confidence level. In the LSCWA, the time series do not have to be equally spaced and equally weighted, and they do not need to have the same sampling rate. The LSCWA can analyze non-stationary time series consisting of constituents of variable amplitude and frequency variability over time.

When analyzing unequally spaced time series, spectral leakages appear in the spectra and spectrograms (i.e., energy leaks from one spectral peak into another). However, the spectral leakages can be significantly mitigated by simultaneous suppressing the significant peaks as done in the LSSA and LSWA. In the LSCWA, the effect of the leakages can be further mitigated because they appear randomly in the spectrograms of each time series. Therefore, their cross-spectrogram mainly shows the coherency of the true signals. Furthermore, if by any chance the random errors (e.g., colored noise) that might be present in two time series appear to have similar behavior in some time periods, then they may also contaminate the cross-spectrograms.

The time series analyses presented in this paper are concrete examples of real time series which are sampled at different rates and represent time-variant systems where the Fourier transform and wavelet transform or other traditional methods cannot be applied directly. In geophysical time series analysis, there are also cases in which time series show discontinuities, for example in GPS (global positioning system) coordinate time series that may have discontinuities (i.e., sudden offset or "jump") in its values or trend due to tectonic phenomena. Such cases are also observed in time series of gravimeter measurements. Since the LSWA and LSCWA decompose time series segment-wise (depending on the time and frequency), selecting $\underline{\mathbf{\Phi}} = [\mathbf{1}, \mathbf{t}]$ for constituents of known forms will automatically consider the discontinuities simultaneously with the periodic constituents thus, producing more reliable results for the spectral peaks.

Finally, in many applied sciences, researchers would like to study the impact of one phenomenon on another by analyzing two or more time series (or data series that are measurements recorded over other quantities such as distance instead of time, e.g., seismic data series) obtained for each phenomenon. The LSCWA is a useful tool that can efficiently and directly show the coherency and phase differences between the time series to make a reliable decision.

8 Acknowledgement

This research has been financially supported by Natural Sciences and Engineering Research Council of Canada (NSERC), Pacific Institute for the Mathematical Sciences (PIMS) and partially by Carbon Management Canada (CMC).

Appendix 1: A decimation algorithm using the Gaussian filter

Since the time series in the XWT must have the same sampling rates, the GGT trace series described in Sect. 5.2 must be decimated from 3600 to 360 samples per hours. In this appendix, we show how one may decimate the GGT trace series for the first satellite track shown in Fig. 5a.

To decimate the M value of the original GGT trace series and show the importance of considering the covariance matrix of decimated data points, we use the Gaussian function $g(\ell) = e^{-0.5\ell^2/\sigma^2}$, where $\sigma = 2.5$ and $-9 \leq \ell \leq 9$. In other words, the Gaussian window contains 19 samples (Fig. 13a). Thus, the cut-off frequency is (sampling rate)$/(2\pi \cdot \sigma)$ that is $3600/(2\pi \cdot 2.5) \approx 229$ c/h. The Gaussian function is normalized to define the weights of the filter as $w(\ell) = g(\ell)/s$ $(-9 \leq \ell \leq 9)$, where $s = \sum_{\ell=-9}^{9} g(\ell)$. It can be seen from Fig. 13a that the Gaussian windows overlap each other when translate 10 points over time (red arrows), and so we may obtain the weighted covariances between the decimated data points using the weights shown with solid black diamonds.

The weighted average and standard deviation of the GGT trace values within each window give the value of the decimated data point and its error bar, respectively (e.g., Pagiatakis et al. 2007). More precisely, suppose that n is the number of data points in the original GGT trace series $f(t_i)$ $(1 \leq i \leq n)$, and m is the number of data points in the decimated GGT trace series $h(\tau_j)$ $(1 \leq j \leq m)$. In this example, we have $n = 701$ and $m = 71$. We calculate the values of the decimated series as

$$h(\tau_j) = \sum_{\ell=-9}^{9} w(\ell) f(t_{10j+\ell-9}) \tag{25}$$

for $2 \leq j \leq 70$ (except for $j = 1$ and $j = 71$ that correspond to the margins), and their corresponding

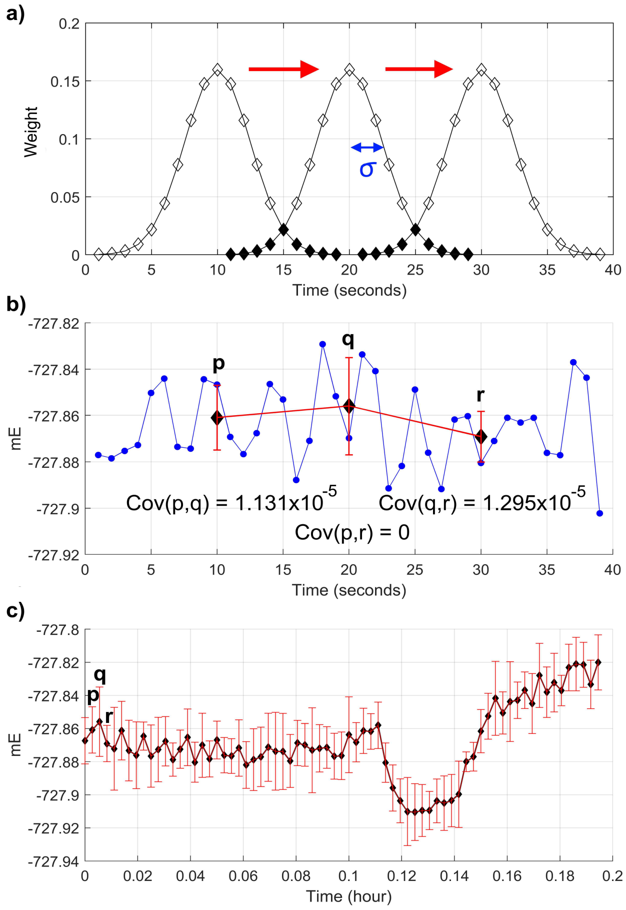

Fig. 13 The decimating process of the GGT trace series for the first satellite track shown in Fig. 5a using a Gaussian window: (a) The translating Gaussian window, (b) The result of decimation of the first 40 data points of the GGT trace series using the Gaussian weights shown with diamonds in panel a (note that p, q, r are the second, third, and fourth decimated points, respectively), and (c) The decimated GGT trace series and its error bars

variances as

$$\mathrm{Var}(j) = \eta \sum_{\ell=-9}^{9} w(\ell)\big(f(t_{10j+\ell-9}) - h(\tau_j)\big)^2, \tag{26}$$

where $\eta = 19/18$ (West 1979). From Eqs. (25) and (26), one may calculate $h(\tau_1)$ (for $j = 1$) and $h(\tau_{71})$ (for $j = 71$) and their variances by ranging ℓ from 0 to 9 and -9 to 0, respectively. One may also use $\eta = 1/\big(1 - \sum_{\ell=-9}^{9} w^2(\ell)\big)$ that is slightly smaller than 19/18, producing almost the same final results (e.g., Galassi et al. 2016). The minimum, maximum, and mean values of the standard deviations (error bars) are 0.006, 0.0257, and 0.0154, respectively. Now it can be seen from Fig. 13a that only the covariance between every two consecutive decimated data points is nonzero when $\sigma = 2.5$. One may also calculate the covariance between each two consecutive decimated data points using

$$\mathrm{Cov}(j, j+1) = \eta_c \sum_{\ell=1}^{9} \Big(w_c(\ell)\big(f(t_{10j+\ell-9}) - h(\tau_j)\big) \big(f(t_{10j+\ell-9}) - h(\tau_{j+1})\big)\Big), \tag{27}$$

for $1 \le j \le 70$, where $w_c(\ell) = w(\ell - 10)$ for $1 \le \ell \le 5$, $w_c(\ell) = w(\ell)$ for $6 \le \ell \le 9$, and η_c may be calculated as $\eta_c = 1/\big(1 - \sum_{\ell=1}^{9} w_c^2(\ell)\big)$ similar to η (e.g., Stuart and Ord 2010; Galassi et al. 2016). We illustrate the result of this decimating method for the first few data points and the entire decimated GGT trace series along with its error bars in Fig. 13b and c, respectively (see decimated points p, q, r). The variances and covariances calculated from Eqs. (26) and (27) form a covariance matrix (symmetric and tridiagonal) associated with the decimated GGT trace series.

References

Abd El-Gelil M, Pagiatakis S D (2009) Least-squares self-coherence for sub-nGal signal detection in the superconducting gravimeter records. J Geodynamics 48 (3):310-315. doi: 10.1016/j.jog.2009.09.018

Abd El-Gelil M, Pagiatakis S D, El-Rabbany A (2008) Frequency-dependent atmospheric pressure admittance of superconducting gravimeter records using least-squares response method. Phys Earth Planet Inter 170 (1-2):24-33. doi:10.1016/j.pepi.2008.06.031

Amato U, Antoniadis A, Pensky M (2006) Wavelet kernel penalized estimation for non-equispaced design regression. Stat Comput 16(1):3755. doi:10.1007/s11222-006-5283-4

Amm O (1997) Ionospheric Elementary Current Systems in Spherical Coordinates and Their Application. J geomagnetism and geoelectricity 49(7):947-955

Amm O, Viljanen A (1999) Ionospheric disturbance magnetic field continuation from the ground to the ionosphere using spherical elementary current systems. Earth, Planets and Space 51(6):431-440

Brown R G, Hwang P Y C (2012) Introduction to random signals and applied Kalman filtering. 383. John Wiley and Sons, Inc, New Jersey, U.S.A.

Campbell J (2004) VLBI for geodesy and geodynamics, The role of VLBI in astrophysics, astrometry and geodesy, Chap. 22, NATO Science Series II: Math Phys Chem (135):359-381

Craig A T, Hogg R V and McKean J (2013) Introduction to mathematical statistics (7th Edition), pp. 694, Pearson

Craymer M R (1998) The least-squares spectrum, its inverse transform and autocorrelation function: Theory and some application in geodesy. Ph.D. Thesis, University of Toronto, Canada

Foster G (1996) Wavelet for period analysis of unevenly sampled time series. Astron J 112(4):1709-1729

Ge Z (2008) Significance tests for the wavelet cross spectrum and wavelet linear coherence. Ann Geophys 26(12):3819-3829. doi: 10.5194/angeo-26-3819-2008

Galassi M, Davies J, Theiler J, Gough B, Jungman G, Alken P, Booth M, Rossi F, Ulerich R (2016) GNU Scientific Library. Reference Manual, Edition 2.3, for GSL Version 2.3, 9 December 2016, 612 pp

Glen A G, Leemis L M, Drew J H (2004) Computing the distribution of the product of two continuous random variables. Computational Statistics and Data Analysis 44(3):451-464

Ghaderpour E, Pagiatakis S D (2017) Least-squares wavelet analysis of unequally spaced and non-stationary time series and its applications. Math Geosci. 49(7): 819-844 doi: 10.1007/s11004-017-9691-0

Grinsted A, Moore J C and Jeverjeva S (2004) Application of the cross wavelet transform and wavelet coherence to geophysical time series. Nonlinear Processes in Geophysics 11:561-566

Gupta A K (2004) Handbook of beta distribution and its applications. CRC Press. ISBN 978-0824753962

Hazewinkel M (2001) Gauss-Kronrod quadrature formula, Encyclopedia of Mathematics, Springer. ISBN 978-1-55608-010-4

Ince E S (2016) GOCE gradiometer disturbances and their modeling by means of ionospheric dynamics, PhD thesis, York University

Ince E S, Pagiatakis S D (2016) Effects of space weather on GOCE electrostatic gravity gradiometer measurements, J Geodesy, 90(12):1389-1403

Kay S M, Marple S L (1981) Spectrum analysis- A modern perspective. Proc. IEEE 69 (11):1380-1419. doi:10.1109/PROC.1981.12184

Kelley M C (2009) The Earth's Ionosphere: Plasma Physics and Electrodynamics (Vol. 96). Academic press

Mallat S (1999) A Wavelet tour of signal processing. 637. Academic Press, Cambridge UK

Mathias A, Grond F, Guardans R, Seese D, Canela M, Diebner H H (2004) Algorithms for Spectral Analysis of Irregularly Sampled Time Series. J Stat Softw 11(2), p. 27. doi: 10.18637jss.v011.i02

Moler C B (2008) Numerical computing with MATLAB. SIAM. ISBN: 9780898716603

Pagiatakis S, Yin H, Abd El-Gelil M (2007) Least-squares self-coherency analysis of superconducting gravimeter records in search for the Slichter triplet. Phys Earth Planet Inter 160(2):108-123. doi:10.1016/j.pepi.2006.10.002

Pagiatakis S (1999) Stochastic significance of peaks in the least-squares spectrum. J Geodesy 73(2):67-78. doi:10.1007/s001900050220

Peterseim N, Schlicht A, Stummer C, Wiyong Y (2011) Impact of Cross Winds in Polar Regions on GOCE Accelerometer and Gradiometer Data. 4th International GOCE User Workshop, Munich, Germany

Rummel R, Yi W, Stummer C (2011) GOCE gravitational gradiometry. J Geodesy 85(11):777-790. doi:10.1007/s00190-011-0500-0

Shampine L F (2008) Vectorized adaptive quadrature in MATLAB. J of Computational and Applied Mathematics 211(2):131-140. doi: 10.1016/j.cam.2006.11.021

Siemes C, Haagmans R, Kern M, Plank G, Floberghagen R (2012) Monitoring GOCE gradiometer calibration parameters using accelerometer and star sensor data: methodology and first results. J Geodesy. doi: 10.1007/s00190-012-00545-8

Stuart A, Ord K (2010) Kendall's Advanced Theory of Statistics, Distribution Theory I, 6th edition, Wiley. ISBN 0470665300

Stummer C, Siemes C, Pail R, Frommknecht B, Floberghagen R (2012) Upgrade of Level 1b gradiometer processor. ASR 49(4):739-752. doi: 10.1016/j.asr.2011.11.027

Torrence C, Compo G P (1998) A practical guide to wavelet analysis. Bull Am Meteorol Soc 79(1):61-78

Vanicek P (1969) Approximate spectral analysis by least-squares fit. Astrophy Space Sci 4(4):387-391. doi: 10.1007/BF00651344

Wells D E, Vanicek P, Pagiatakis S D (1985) Least-squares spectral analysis revisited. 68 Tech Rep 84, Department of Surveying Engineering, University of New Brunswick, Canada

West D H D (1979) Updating mean and variance estimates: an improved method, Communications of the ACM 22(9): 532-535

Weygand J M, Amm O, Viljanen A, Angelopoulos V, Murr D, Engebretson M J, Gleisner H, Mann I (2011) Application and validation of the spherical elementary currents systems technique for deriving ionospheric equivalent currents with the North American and Greenland ground magnetometer arrays. J Geophysical Research: Space Physics 116(A3):1978-2012

Wresnik J, Haas H, Boehm J, Schuh H (2007) Modeling thermal deformation of VLBI antennas with a new temperature model. J Geodesy 81(6):423-431. doi:10.1007/s00190-006-0120-2

Yi W, Rummel R, Gruber T (2013) Gravity Field Contribution Analyses of GOCE Gravitational Gradient Components. Studia Geophysical et Geodetica 57(2):174-202